RESEARCH ARTICLE

ADVANCED SENSOR RESEARCH Open Access

www.advsensorres.com

Bromine-Enhanced Organic Materials for X-ray Sensors: Unveiling the Potential of Small Molecules and Polymers through Material Design and Film Fabrication

Rokas Dobužinskas, Andrius Poškus, Vygintas Jankauskas, Mindaugas Viliūnas, Egidijus Kamarauskas, Marytė Daškevičienė, Vytautas Getautis, Kęstutis Arlauskas, and Darius Abramavičius**

"With deep gratitude, to my esteemed former supervisor, Kęstas (Kęstutis Arlauskas), a renowned figure in the physics community whose unwavering dedication to teaching and research has significantly impacted the trajectory of numerous students and colleagues, including myself." – Rokas.

Organic X-ray sensors are a promising new class of detectors with the potential to revolutionize medical imaging, security screening, and other applications. However, the development of high-performance organic X-ray sensors is challenged by low sensitivity. This paper reports on the development of nine X-ray sensors based on new organic materials. It is demonstrated that the incorporation of bromine atoms into the sidechains of carbazolyl-containing organic molecules significantly enhances their X-ray sensitivity. This research suggests that incorporating a variety of high-atomic-number chemical elements into well-established organic semiconductors is a promising strategy for designing efficient X-ray sensor materials.

1. Introduction

Everyday life extensively relies on organic compounds, which remain indispensable in numerous applications in addition to the small carbon footprint they generate.[1–5] Organic chemistry flourishes by leveraging physical methods to characterize properties and by refining the latest advancements in synthesis.[6–9] Organic electronics has been a hot research topic for over two decades, and as a result, it is gaining a significant role in modern industry. Thin film electronics, roll-to-roll technologies, and biocompatible organic devices[10–16] found applications in electronics, healthcare, and overall environmental monitoring as sensing materials, and many more are expected to emerge as "smart" common appliances in the future.

Well-established X-ray sensors in the industry heavily rely on modern electronics fabrication methods. Consequently, most applications utilize silicon-based materials, ranging from high-precision Si(Li) detectors to flat-panel amorphous Si devices.[17–19] Flat-panel technology, exemplified by mammography systems, experienced a breakthrough in the early 2000s due to the successful incorporation of amorphous selenium (a-Se) as an absorptive layer within transistor arrays.[20] While direct X-ray absorption materials are considered the industrial standard for premium devices, their high cost arises from the need to balance efficient X-ray absorption with optimal electrical properties. Although several heavy element materials, such as CdTe, PbO, and HgI_2, have been proposed as more X-ray-absorbent and potentially lower-cost alternatives, they have yet to displace traditional devices.[21]

Another approach involves indirect detection, where X-rays are converted into light by scintillator materials like gadolinium oxysulfide (Gd_2O_2S) or cesium iodide (CsI). The photodiode then detects this light and converts it into an electrical signal. While scintillator materials might be easier to integrate into the manufacturing process, potentially leading to higher detection efficiency, the final image resolution may suffer.[22–24] Recently, organic phosphors have been shown to be excellent scintillators, rivaling industry standards.[25] However,

R. Dobužinskas, A. Poškus, V. Jankauskas, M. Viliūnas, E. Kamarauskas, K. Arlauskas, D. Abramavičius
Institute of Chemical Physics
Faculty of Physics
Vilnius University
Saulėtekio av. 3, Vilnius 10222, Lithuania
E-mail: rokas.dobuzinskas@ff.vu.lt; darius.abramavicius@ff.vu.lt
M. Daškevičienė, V. Getautis
Department of Organic Chemistry
Faculty of Chemical Technology
Kaunas University of Technology
Radvilėnu pl. 19, Kaunas 50254, Lithuania

The ORCID identification number(s) for the author(s) of this article can be found under https://doi.org/10.1002/adsr.202400018

DOI: 10.1002/adsr.202400018

our investigation in this work focuses solely on direct conversion.

Developments in high-energy irradiation sensing by organic materials mark a compelling frontier where the principles of organic chemistry converge with the precision demands of radiographic (e.g., in X-ray) detection. Traditional inorganic semiconductor materials are well established in the industry, although organic sensors are shown to detect and capture X-ray photons with enhanced sensitivity, ease of manufacture, and overall adaptability.[26–41] The creation of new organic compounds combined with cutting-edge sensor technology paves the way for fresh opportunities in both medical diagnostics[42–44] and nondestructive environmental testing.[45–47]

Since the discovery of photoconductivity in poly(9-vinylcarbazole) (PVK), derivatives of carbazole have become the subject of many investigations among materials scientists.[48] Recently, in some fields of application, PVK has been replaced by carbazole-containing oligomers. Carbazolyl-containing oligoethers, particularly poly[9-(2,3-epoxypropyl)carbazole] (PEPK), are known as fairly effective organic photoconductors used in electrophotography for the manufacture of microfilms, microfiches, colored slides, and in the photothermoplastic recording of information.[49] Gaidelis et al.[50,51] reported that the carrier mobilities of PEPK are by more than one order of magnitude higher than the values reported for PVK. Unfortunately, PEPK, like many polymeric materials, exhibits polydispersity with respect to molar mass and end groups and the possibilities of its purification are limited. The impurities trap charge carriers and lead to a decrease in the device's efficiency and shortening of its lifetime. On the other hand, thorough purification of molecular glasses can be performed by such methods as sublimation, crystallization, chromatography, etc., and this is a serious advantage over polymeric materials. Well-defined branched carbazolyl-containing photoconductive compounds with low molar mass and with the ability to form amorphous films on substrates, including flexible ones, were synthesized in the 1980s for application in electrophotography. They were produced by the reactions of glycidyl ethers containing photoconductive groups with different bifunctional compounds, such as aromatic diols, dimercapto compounds, and derivatives of aniline.[52–54] Such branched molecules can be chemically crosslinked in the layer, for example, by reaction of the hydroxyl groups with polyisocyanates to produce layers that would be mechanically stable for decades, and maintain superior mobility of charge carriers.

The X-ray absorption of a material, described by the attenuation coefficient (X), exhibits a pronounced dependency on the atomic number (Z). This relationship is expressed as Z: $X \approx Z^4 / E^3$ with E denoting the X-ray photon energy.[55] Unfortunately, simple hydrocarbon compounds, comprising most organic molecules, manifest inadequately low-Z atomic numbers, and thus, low photoelectric absorption coefficient for the photon energies employed in medical X-ray applications.[56] One possible approach to tackling this problem is based on mixing or blending organic charge-transporting materials with specific X-ray absorbing compounds. However, such active materials have complex internal morphology, which is prone to molecular diffusion, phase separation, and thus degradation. The layers thus are not stable in ambient conditions.[57–59]

Alternatively, advancements in synthesis methodologies enabling the incorporation of high atomic number elements into the organic molecules present a viable solution. This enhances the absorption while maintaining a stable internal molecular structure. As a result, stable, predictable, and relatively thin active layers could be produced with appreciable sensitivity to X-ray irradiation.

In this paper, we characterize nine different organic compounds as potential X-ray sensing films. The triphenylamine-based and carbazolyl-containing branched molecules were solution-cast onto a glass substrate with indium tin oxide (ITO) and aluminum electrodes. We investigated the electrical characteristics of the films in the dark and under exposure to X-rays. Calculated quantum efficiencies, Monte Carlo simulations of charge carrier generation and mobility, provided measurements of highest occupied molecular orbit (HOMO) and lowest unoccupied molecular orbit (LUMO) levels, and the data from X-ray direct detection measurements suggest that the X-ray sensitivity of organic materials can potentially be enhanced by incorporating bromine functional groups.

2. Results and Discussion

2.1. Experimental Results

The sample structure, including the ITO layer and the molecular films, is schematically illustrated in **Figure 1**. The detailed procedure for creating and measuring the films, as well as the synthesis of organic molecules, is described in the Experimental Section.

Briefly, organic films were deposited onto 1 mm thick glass substrates pre-coated with an ITO layer. To achieve consistent film thickness, the same volume of the prepared solutions was evenly drop-cast onto the entire area of each substrate, allowing the solvent to fully evaporate for 1 h. Following solvent removal, the final layer thickness reached ≈20 μm, as detailed in Table 2 of the Experimental Section. Subsequently, a top aluminum electrode, 40 nm thick, was deposited via vacuum evaporation using a mask enclosure. This process formed circular electrodes with a diameter of 3 mm on the active area. Each substrate had dimensions of 15 mm × 25 mm, allowing for five electrodes with an area of 0.07 cm^2 to be placed on each substrate. The results are provided from the electrodes located on the active areas of each sample, with the same pattern repeated for each electrode.

The organic molecules have their chemical structures presented in **Figure 2**. These molecules contain either triphenylamine or carbazolyl functional groups. Triphenylamine-containing molecules used in this study are only two—functionalized with double (2TPA) and triple (3TPA) triphenylamines (see Figure 2). All other molecules in the study are functionalized with carbazolyl groups which can be again classified in subgroups—without bromine (a small chain polymer PEPK and small molecules KONF, KOS), and containing four bromine atoms in a molecule (4Br-KPON and 4Br-KOO), and with eight bromine atoms (8Br-KONF and 8Br-KOS). 4Br-KPON has also phenyl groups. The number of bromine atoms defines the concentration of bromine in the final sample. Notably, the mass density is similar across these materials because the molecules are comparable in size, weight, and total number of atoms. There-

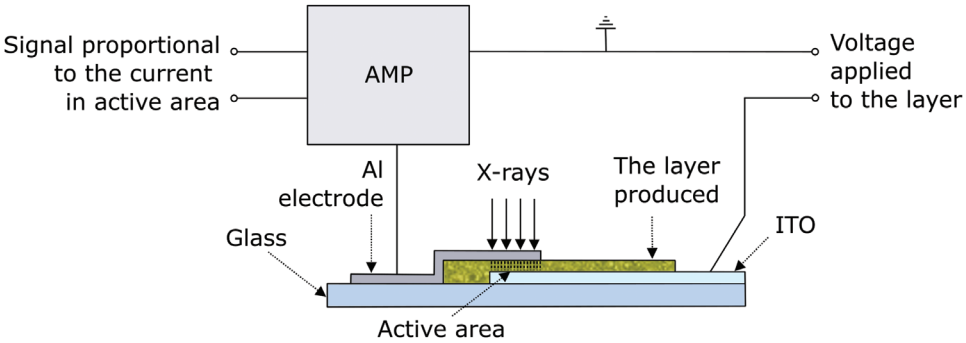

Figure 1. Experimental instrumentation, sample, and measurement circuit.

fore, focusing on the count of Br atoms per molecule (either 0, 4, or 8) offers the most straightforward approach to characterize and compare the materials (the molar ratio of Br is respectively ≈0, 3, or 6 mol%). X-ray absorption and quantum efficiency (*QE*) of different molecule layers are described further in the Discussion section.

The *I*–*V* curves were measured by applying a voltage to the ITO electrode and measuring the induced current through the Al electrode with a transimpedance amplifier and a 1 GΩ feedback resistor. The X-ray photocurrent was obtained by irradiating the samples with a molybdenum target X-ray tube at 35 kV and 1 mA, which induced the 17.5 keV K_α characteristic radiation in the middle of the continuous spectrum of bremsstrahlung radiation. The measurements were conducted in the dark and under X-ray irradiation, and the current values were ±0.5 pA accurate. The applied voltage ranged from −300 to 300 V, creating an electric field of ±150 kV cm^{-1} across the film.

Figure 3 presents the *I*–*V* curves in the dark conditions. Due to the difference in work functions between the ITO and Al electrodes, the *I*–*V* curves are slightly asymmetric for some materials (8Br-KONF, 2TPA, 3TPA), but this is not the case for most materials (PEPK, KONF, KOS, 4Br-KOO, 8Br-KOS). The maximum dark current (I_{dark}) in the reverse bias is 200 nA for 8Br-KOS while it is equal to 300 nA in the forward bias for 3TPA. At most of the voltage values, the *I*–*V* characteristics range from 1–10 to 100 pA in the range of experimental voltage. Note that at an even lower voltage (100 V), a significant number of materials (KONF, KOS, 4Br-KOO, 8Br-KONF 2TPA, 3TPA) can operate in the dark with currents up to 10 pA. Our experimental results show that most measured currents fall below the industry standard of 10 pA mm^{-2} (adjusted for the active area of our sample it is 70 pA). which is required for X-ray detection devices at low voltage conditions (e.g., 5 or 12 V).

Photocurrent (I_{ph}) is defined as the difference between the current $I_{x\text{-}ray}$ measured under X-ray exposure and the dark (I_{dark}) current ($I_{ph} = I_{x\text{-}ray} - I_{dark}$) and it is presented in **Figure 4**. By comparing photocurrents under forward and reverse bias voltages, we observe that all materials exhibit photocurrent mismatch. This means that the photocurrent is higher under forward bias voltage than under negative voltage. The Al-ITO electrode structure is likely responsible for this difference in photocurrent. Some materials do not reach 10 pA in the whole range of voltages (KOS, KONF, 8Br-KOS, 8Br-KONF). The 2TPA has a photocurrent greater than 10 pA in the forward bias but is significantly smaller in the negative bias. The highest photocurrent is detected for 4Br-KPON, 3TPA, and 4Br-KOO materials. The largest photocurrent was detected for 4Br-KPON, which has a top current of 0.6 nA at the forward bias of 300 V, and 0.12 nA in the case of negative bias.

The current enhancement by X-ray exposure can be characterized by the photo-to-dark ratio $I_{x\text{-}ray}/I_{dark}$, presented in **Figure 5**. The overall ratios for most of the materials are below 1, although 4Br-KPON demonstrates ratios up to 8 under 300 V. 3TPA shows also promising results with ratios under the forward bias voltage reaching 4. It should be noted that the ratio for most materials is either decreasing or roughly constant as the voltage is increased. This indicates that the effectiveness is higher at lower voltages—the applications of a lower voltage mode (12 to 48 V) are promising for applications of such materials as X-ray sensors.

In **Figure 6**, the dependence of the X-ray-induced photocurrent on the X-ray flux is measured at 300 V. A linear function (black dashed line) is presented for reference. The figure demonstrates that the device's signal photocurrent is approximately directly proportional to the photon number for all materials. It is noteworthy that deviations from a linear dependence are observed below 2×10^9 cm^{-2} s^{-1} in X-ray flux (see Figure 6). Optimal results are observed above this value. Deviations below 2×10^9 may be affected by the source of the X-ray tube under low cathode current operation.

2.2. Discussion

The simplest designs in using organic polymers or small organic molecules in X-ray-sensitive detectors rely on employing these materials as charge-transporting layers, while X-ray absorption and photocurrent generation can be achieved by additional ingredients (e.g., inorganic nanoparticles, or specific scintillators)[25] dispersed in the polymer. Incorporation of halogen atoms in scintillators may enhance their luminescence sensitivity. However, in such conditions, the properties of the active layers become dependent on the morphology of the blends. This may result in material degradation due to complexation/crystallization during the device's operation. In the present study, we describe properties of materials where charge transporting and X-ray absorbing (via high-Z elements) properties are incorporated at the very molecular level. This is advantageous because material composition at the molecular level becomes well organized, and interatomic dis-

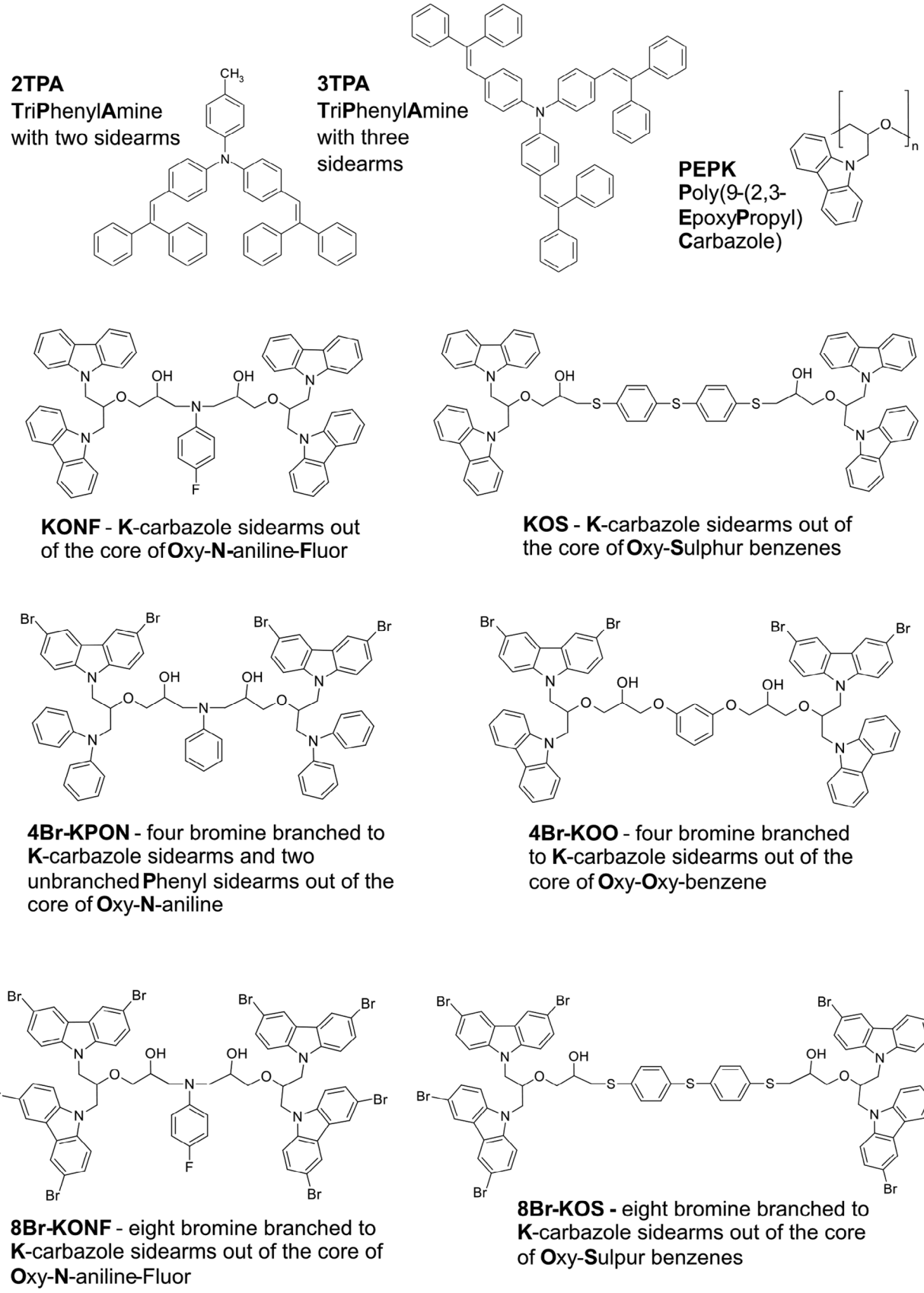

Figure 2. The chemical structures of organic compounds used in the production.

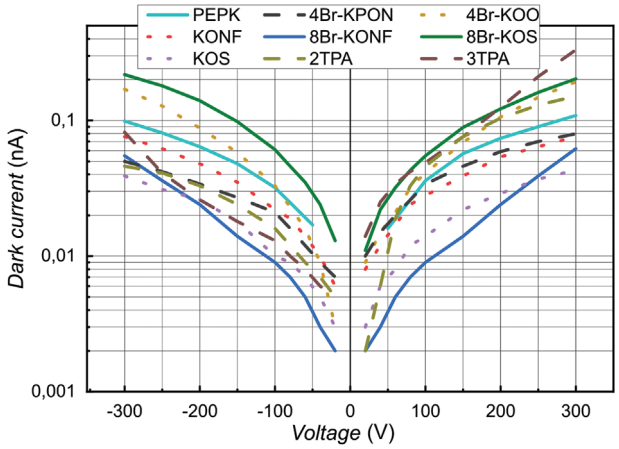

Figure 3. Current–voltage characteristics of the layers produced. The type of active materials is defined in the inset.

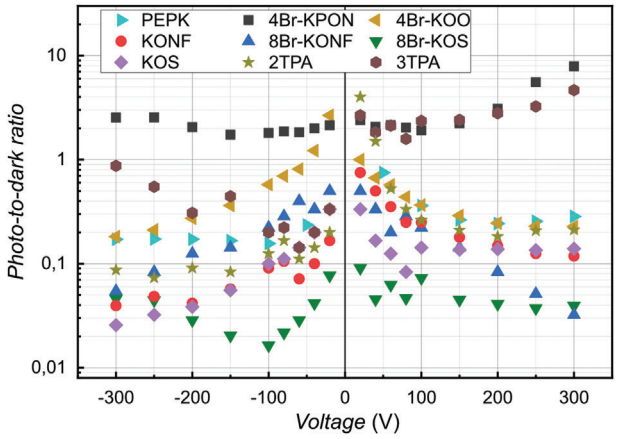

Figure 5. Voltage dependence of the X-ray-induced photo-to-dark ratios.

tances are well defined. There are various approaches that combine absorptive elements with organic materials including those based on scintillators.[25] Similar to our purely organic approach, the article mentions incorporating halogen atoms as an example for enhancing the X-ray absorption capabilities of organic scintillators themselves. By using scintillator materials, you can overcome the "charge transfer" problem by limiting absorption exclusively to the luminescent part of the detector. Achieving high sensitivity often necessitates the use of highly luminescent materials.

However, this presents a significant chemical challenge for both scintillator-based and direct conversion detectors. Incorporating high-Z atoms (heavy elements) into organic materials (typically composed of low-Z elements) requires specific synthetic steps to ensure efficient integration of the heavy elements. Such element combinations are not widely used in organic chemistry.

Another promising area for achieving direct absorption lies in metal-organic frameworks (MOFs),[60] which are crystalline hybrid materials consisting of metal centers linked by organic molecules forming well-structured frameworks, are promising materials that bind together heavy atoms with organic materials. Another class of materials, which are considered in this paper, is obtained by halogenation of organic compounds,[61] where heavy halogen atoms can be embedded into polymers.[62] Such design leads to organic materials, which are highly sensitive to ionizing irradiation and maintain desirable electric characteristics. The possibilities for creating different molecules are wide, but these possibilities are narrowed by the need for the molecules to be stable at room temperature and to withstand the solution processing used in the industrial production of sensor films.

In the present study, the focus is on producing a stable material with superior electrical properties. We have carefully selected organic compounds for this study to analyze and compare how the sidechains of different molecule structures influence the induction of X-ray photocurrent. While many previous studies have focused on organic compounds with carbazolyl molecules, these have mainly been popular choices for use in organic solar cells or OLEDs.[63–66] In our case, considering the charge carrier mobility of molecules like triphenylamine (2TA and 3TPA), they emerge as promising candidates for successful charge extraction. However, it is crucial to note that carrier mobility alone is not the sole determinant of photocurrent. Charge injection plays a pivotal role in defining both dark current and photocurrent levels.

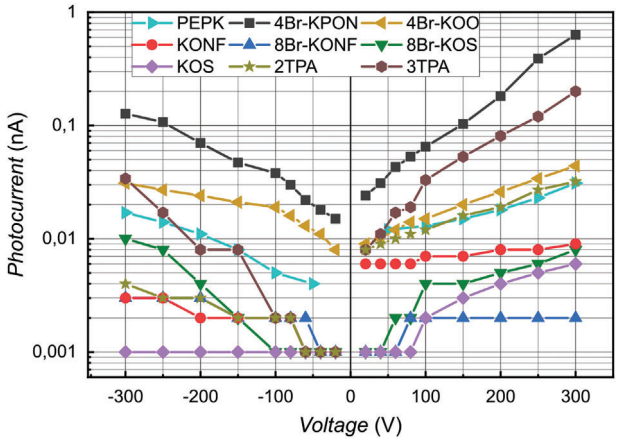

Figure 4. Voltage dependence of X-ray-induced photocurrent under a dose rate of 13.3 mGy_{air} s^{-1}.

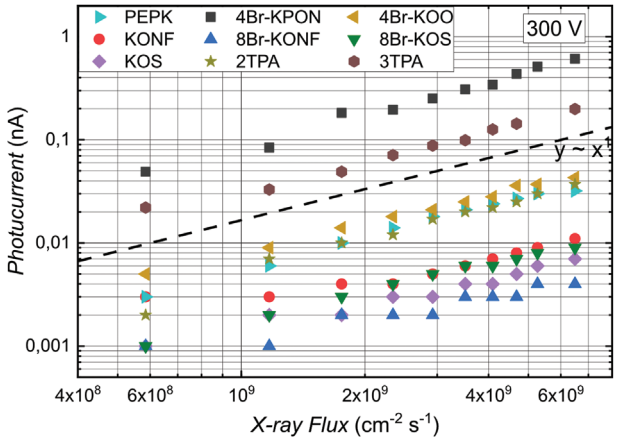

Figure 6. X-ray flux dependence of the X-ray-induced photocurrent at 300 V applied to the layers.

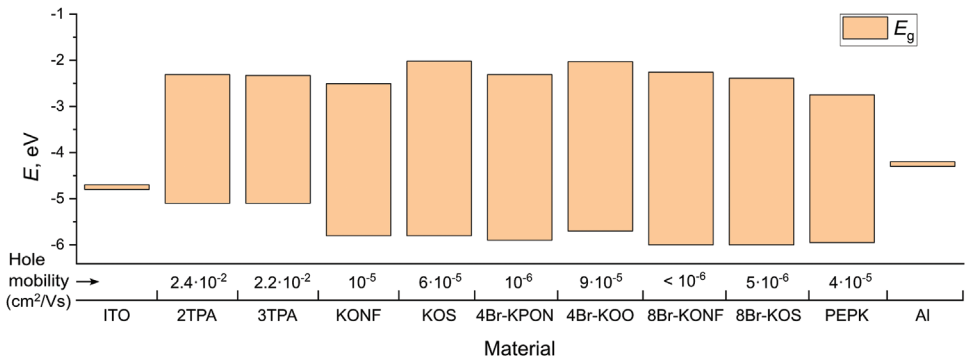

Figure 7. The energy bandgaps of the organic materials (columns) and work functions of electrodes (lines). Hole mobilities are listed underneath the columns, respectively aligned with the names of the materials. The electrographic measurement details are provided in the Experimental Section.

Electrode selection plays a crucial role in optimizing X-ray sensor performance. Light-transparent electrodes, like ITO and FTO (Figure 1), are widely used due to their established role in solar cells and OLEDs, offering excellent light transmission and pre-patterned availability on glass substrates for laboratory convenience. For top electrodes, metals, like Al, Cu, Ag, and Au, are commonly employed via vacuum evaporation. Perovskite X-ray sensors typically utilize the ITO/Au configuration for direct X-ray absorption. In this work, we opted for the ITO/Al configuration due to its practicality in film production. While ITO/Au is a viable option, it presents a potential risk—the high melting point (1064 °C) and atomic weight (197 g mol^{-1}) of Au compared to Al (660 °C, 27 g mol^{-1}) can lead to deeper penetration into the underlying organic material (typically melting around 100 °C), potentially compromising its stability and device performance reliability. Additionally, Au, being a high-Z metal, might alter the results of the examined material by forming nanoparticles within its bulk.[67] Conversely, Al's work function, positioned within the material's bandgap, contributes to an exceptionally low dark current (desirable), but at the expense of lower charge extraction efficiency during X-ray exposure.

After the charge is generated by X-rays, it must be extracted by an electric field. In organic compounds, usually, holes are the charge carriers, where their mobility is higher and takes an important role making the charge not to recombine and reach the electrodes. On the other hand, minor carriers, such as electrons, determine the magnitude of the photocurrent because photocurrent is generated by X-ray-induced photoeffect. Using the electrode configuration of ITO-Al diode-type characteristics may be expected, and the charge extraction for certain types of carriers may be enforced. The effectiveness of carrier extraction in such an electrode array depends on the HOMO and LUMO energy levels of a molecule (**Figure 7**). Consider, for example, the influence of the HOMO position, particularly on the *I–V* characteristics in the dark for triphenylamine-type molecules (2TPA and 3TPA in Figure 3). This is because holes can more easily inject into the HOMO (with an energy level of −5.1 eV) from ITO, which has a work function of 4.7 eV (Figure 7). On the contrary, for another group of materials with carbazolyl-type functional groups, the HOMO is lower, approximately −6 eV, including the polymer PEPK. PEPK has a considerably lower LUMO level (−2.8 eV) than the LUMO energy levels of other materials, including those with triphenylamines, which range from −2 to −2.5 eV. This creates a significant barrier for electrons from both ITO and Al electrodes. Consequently, carbazolyl-type molecules exhibit comparable barriers for both electrons and holes due to the work function of ITO and Al lying in the middle of the bandgaps (E_g in Figure 7). These barriers, along with the bandgap and work function of an electrode material, fundamentally contribute to the dark current in the samples.

While the proposed model offers valuable insights, it cannot fully explain all the observed results. The strength of the molecule-substrate interaction varies between materials, and this variation can influence the current–voltage (*I–V*) characteristics. Materials, particularly those exhibiting a current below 10 pA (e.g., 3TPA and 8Br-KOS in our study), may exhibit lower dark and photocurrents at lower voltages, especially under reverse bias applied to the ITO electrode. This phenomenon is likely caused by insufficient contact between the ITO electrode and the organic layer due to poor adhesion. This effect might be less pronounced at higher voltages as charge carriers are extracted from a larger volume of the film. It is noteworthy that the quality of the produced film might not directly influence long-term stability. This is supported by our previous study on similar small-molecule materials, which demonstrated long-term stability.[68] However, for ionizing radiation detectors, the long-term performance, particularly stability, is likely connected to the chemical structure of the material.[69]

In order for an X-ray photocurrent to be induced in the sample, the incident X-ray photons must be absorbed by the material and create free-charge carriers. The ability of each material to absorb X-ray radiation is characterized by the absorption QE, which is expressed by the equation

$$QE = \left(1 - e^{-X\rho x}\right) \times 100\% \quad (1)$$

where X is the attenuation coefficient, which can be obtained from the database NIST.GOV,[70] and ρ and x are the density and thickness of the material. The theoretical absorption quantum efficiencies calculated for the materials used in this work are presented in **Figure 8a**. The inset shows the region around the characteristic peak of the molybdenum X-ray tube at 17.5 keV.

Since the absorption QE is proportional to the fourth power of the material's atomic number Z (QE $\sim Z^4 / E^3$), it is advisable for the material to contain as many large-Z atoms as possible. While many studies have utilized lead ($Z = 82$) monocrys-

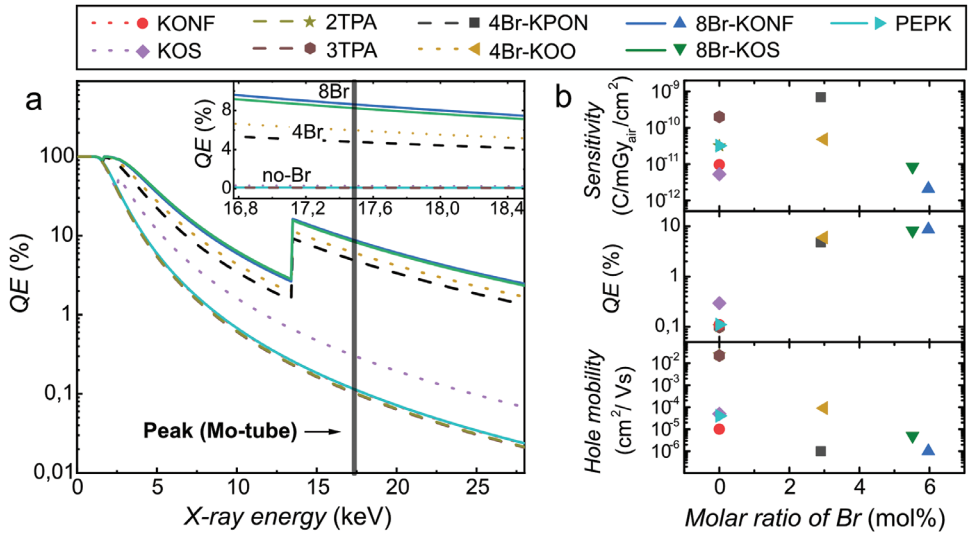

Figure 8. Characters of the films. a) Theoretical quantum efficiency (calculated from NIST.GOV data) for the nine materials used in the experiment (thickness 20 μm). b) Dependence of X-ray sensitivity, quantum efficiency, and hole mobility on the molar ratio of bromine (mol%).

tals and polycrystals, selenium ($Z = 34$) layers are commonly used as the primary absorber in direct X-ray imaging devices in medical institutions. While selenium is very well established, the hybrid organic detectors with high-Z monocrystal nanoparticles demonstrate very promising results outcompeting industrial devices.[40,71,72] On the other hand, our work incorporates elements with atomic numbers similar to selenium (Se) into the molecules. This allows for the development of organic-based sensors containing bromine (Br, $Z = 35$). Br is a higher-Z element, and its presence can significantly enhance quantum efficiency compared to elements typically found in organic compounds, such as hydrogen (H), carbon (C), nitrogen (N), fluorine (F), and sulfur (S), which have atomic numbers of 1, 6, 7, 9, and 16, respectively.

This leads to the X-ray sensitivity of the molecular film, a crucial parameter defining sensor performance. Sensitivity is defined as the charge collected per dose rate describes the ability to detect X-rays. However, the lowest detectable dose defines another parameter: the detection limit (details for each molecule are presented in **Table 1**). In our study, sensitivity and detection limit are correlated and linked to film performance. This means that a higher photocurrent (or sensitivity) translates to a lower detection limit, which is a desirable outcome. The lowest detection limit is estimated for 4Br-KPON (0.02 mGy$_{air}$ s^{-1}) while the highest is for 8Br-KONF (6.65 mGy$_{air}$ s^{-1}). This suggests that the issue might not lie with the bromine ionization mechanism (i.e., related not only to X-ray absorption), but rather with the potential for improvement within the molecule itself by enhancing charge generation and extraction.

The surprising result emerges with 4Br-KPON, which exhibits the highest X-ray sensitivity despite having moderate content of bromine (3 mol%) at carbazole sidearms (Figure 8b, top). In contrast, the closely related compound, 4Br-KOO, with slightly different sidearms and an oxy-oxy-benzene core, falls short in terms of sensitivity. Notably, in the materials 8Br-KOS and 8Br-KONF used in this work, which contain the highest amount of the bromine atoms in a molecule are expected to contribute to sensitivity the most because of their highest quantum efficiency (Table 1). However, results of photocurrent indicate that materials with 8Br in the molecule sidearms exhibit lower sensitivity compared to those with 4Br or without it (see Figure 8b). The hole mobilities are similar between carbazolyl-type molecules with 8Br and those with 4Br. However, 8Br materials exhibit lower sensitivity compared to those with 4Br or without it (see Figure 5).

We can additionally correlate sensitivity to two additional factors: quantum efficiency (the amount of X-rays the material

Table 1. Values of quantum efficiency, sensitivity, detection limit, and simulations of maximum photocurrent.

Material	2TPA	3TPA	KONF	KOS	4Br-KPON	4Br-KOO	8Br-KONF	8Br-KOS	PEPK
QE (17.5 keV)	0.101%	0.099%	0.110%	0.295%	4.78%	5.95%	8.61%	8.22%	0.111%
X-ray sensitivity (300 V), C/mGy$_{air}$ cm^{-2}	3.2×10^{-11}	2×10^{-10}	9.6×10^{-12}	5.3×10^{-12}	6.9×10^{-10}	4.8×10^{-11}	2.1×10^{-12}	8.5×10^{-12}	3.2×10^{-11}
Detection limit, [mGy$_{air}$ s^{-1}]	0.443	0.06995	1.477	2.658	0.02045	0.2953	6.645	1.661	0.443
$I_{ph.th}$, [nA]	0.198	0.194	0.179	0.412	4.70	5.77	8.34	8.31	0.188
$I_{ph.th[20\ \mu m]}$, [nA]	0.153	0.153	0.154	0.378	4.87	4.73	8.38	8.22	0.150
$I_{ph.exp}$ (300 V)/$I_{ph.th}$	0.152	0.98	0.050	0.0121	0.138	0.0078	0.00024	0.00096	0.160

can absorb) and hole mobility (the quality of charge transfer). Figure 8b illustrates this comparison for different Br molar ratios. Our results suggest a non-monotonic dependence of sensitivity on Br content. The maximum sensitivity is observed at 3 mol% (achieved by 4Br-KPON), likely due to its increased absorption (higher QE) despite a potential decrease in hole mobility. While sensitivity appears to decrease with increasing Br content beyond 5.5–6 mol% (8Br-KOS and 8Br-KONF), the data is inconclusive regarding the direct negative impact of higher bromine content on hole mobility.

Considering the photo-to-dark ratio, the dark current is approximately linearly dependent on the voltage at low voltages (see Figure 3). The photocurrent (Figure 4) is also linearly dependent on the voltage at low voltages, but then it bends as saturation is approached. In the ideal case, the photocurrent saturates and becomes constant. The photo-to-dark ratio (Figure 5) at low voltages is the ratio of two linear dependencies. If both of these lines pass through the origin (zero), then their ratio is constant. However, the constant value of this ratio does not mean that all photogenerated carriers are extracted. In this case, the photocurrent would already have reached saturation, but it does not. This suggests that significant carrier losses occur due to recombination at low voltages. The decrease in the ratio with voltage increase could be attributed to the approach to saturation: the photocurrent grows slower than linearly (or does not pass through zero), while the dark current continues to rise linearly. For instance, although 4Br-KOO exhibits the lowest photo-to-dark current ratio (see Figure 5), it still shows a positive trend under low voltage. This pattern is observed across all materials. This suggests that high carrier mobility and photogeneration rate are not necessarily the most crucial factors for practical applications, especially for simple devices requiring low voltage operation and only basic radiation indication.

In order to comprehensively evaluate the maximum potential of bromine-enhanced organic materials for X-ray detection, theoretical photocurrent simulations employing the Monte Carlo method were conducted. This method of calculation was preferred to simpler methods in order to take into account energy losses caused by X-ray fluorescence, which can exceed 30% of the kinetic energy released in the material due to the small thickness of the samples and due to existence of high-Z elements in some of them (for a more detailed discussion, see Section 4). The results, along with theoretical quantum efficiency, X-ray sensitivity, and detection limit are presented in Table 1.

The number of free charge carriers generated in the sample per unit time due to incident X-ray radiation is further called "photogeneraton rate" and denoted Φ. It is reasonable to expect that Φ does not depend on external voltage. The value of

$$I_{\mathrm{ph.th}} = \mathrm{e}\Phi \tag{2}$$

is the maximum theoretical photocurrent, which would be measured in the ideal case, when all photogenerated charge carriers reach the electrodes. In practice, however, a part of photogenerated charge carriers are lost due to recombination, so that the experimental photocurrent is less than $I_{\mathrm{ph.th}}$ and depends on voltage. It should approach $I_{\mathrm{ph.th}}$ with increasing voltage because an increase of electric field strength causes shorter drift time and hence causes a reduction of the fraction of photogenerated charge carriers that were lost to recombination. Since the recombination rate is unknown, it is not currently possible to calculate the actual (voltage-dependent) photocurrent theoretically. However, it is interesting to calculate the ratio of the maximum experimental photocurrent (which corresponds to the maximum voltage used in the current work, i.e., +300 V) and the maximum theoretical photocurrent defined above ($I_{\mathrm{ph.th}}$). This ratio has the meaning of the fraction of photogenerated charge carriers that reach the electrodes and thus provides a measure of the "efficiency" of a given material when converting the photogeneration rate into the actual photocurrent at the mentioned value of external voltage.

Since the values of quantum efficiency at 17.5 keV (which are given in Table 1) are less than 10%, photoelectric absorption is approximately uniform over the entire thickness of the layer. This means that the values of Φ and $I_{\mathrm{ph.th}}$ are approximately proportional to the layer thickness. Since the investigated layers have different thicknesses, some of the differences in the values of Φ obtained by Monte Carlo simulations (and the consequent differences of $I_{\mathrm{ph.th}}$) can be caused by differences in the layer thickness. In order to eliminate this effect of the layer thickness, the next-to-last row of Table 1 presents the values of $I_{\mathrm{ph.th}}$ "normalized" to 20 μm, that is, the theoretical photocurrent that corresponds to the layer thickness of 20 μm. In Table 1, this photocurrent is denoted $I_{\mathrm{ph.th[20\,\mu m]}}$. Its values were calculated as follows: $I_{\mathrm{ph.th[20\,\mu m]}} = I_{\mathrm{ph.th}} \times (20\,\mu\mathrm{m}/d)$, where d is the layer thickness. Comparison of the values of $I_{\mathrm{ph.th[20\,\mu m]}}$ shows that the differences of the theoretical photocurrent in some materials (for example, 4Br-KPON and 4Br-KOO, or the four materials that do not contain elements with atomic numbers greater than 9) are mainly caused by differences of their thickness.

The ratios of the maximum experimental photocurrent (at 300 V) to the theoretical photocurrent are given in the fourth row of Table 1 (this ratio is denoted "$I_{\mathrm{ph.exp}}(300\ \mathrm{V})/I_{\mathrm{ph.th}}$"). However, since these values are proportional to the W values (the average energy absorbed per one created electron–hole pair), which are known only very approximately (see Section 4), their uncertainties may be as large as 50%. In the case of 3TPA, this ratio is close to 1. In all other cases, the mentioned ratio is much less than 1, which means that the photocurrent is far from the saturation value, that is, most of the photogenerated charge carriers are lost due to recombination. An increase in electric field strength causes a reduction of the mentioned losses and consequently an increase in the fraction of photogenerated carriers that reach the electrodes. However, the maximum achievable electric field strength is limited by experimental constraints, specifically the breakdown of the film, necessitating the use of a voltage of up to 300 V for the investigation.

The fraction of charge carriers lost to recombination is determined by the ratio of the drift time and the charge carrier lifetime. The drift time is inversely proportional to the product of electric field strength and mobility of charge carriers. It follows that mobility and lifetime of charge carriers are major factors causing the differences in experimental photocurrent in different materials. This partly explains why 2TPA and 3TPA, which are characterized by relatively high mobility (see Figure 5), have relatively large values of the ratio $I_{\mathrm{ph.exp}}(300\ \mathrm{V})/I_{\mathrm{ph.th}}$. In the case of 4Br-KPON and PEPK, the surprisingly large value of $I_{\mathrm{ph.exp}}(300\ \mathrm{V})/I_{\mathrm{ph.th}}$ (despite the relatively low mobility) indicates the importance of the charge carrier lifetime, which is probably much longer in 4Br-

KPON and PEPK than in other mentioned materials (that is to say, the recombination rate is much lower).

3. Conclusion

The dark currents of the organic compounds were measured to be below the industry standard of 10 pA mm^{-2}, indicating their suitability for X-ray detection devices. The incorporation of bromine atoms into the sidechains of carbazolyl-type organic molecules significantly enhances their X-ray absorption, although experimental results show that four bromine atoms functionalized in a molecule is optimal. The highest photocurrents were observed in the materials with 4 bromine atoms in the molecule 4Br-KPON or 4Br-KOO and the material with the highest hole mobility—3TPA. According to the theoretical evaluation of the photocurrent results, the lifetime of charge carriers in 4Br-KPON is the primary factor contributing to its relatively high photocurrent. Conversely, in molecules without bromine (2TPA and 3TPA), the mobility of charge carriers is the key factor influencing photocurrent generation. Theoretical results further suggest that the photocurrent could be enhanced by a factor of 1000 if the charge extraction efficiency of molecules with 8 bromines were optimized. Our study demonstrates that carbazolyl or phenyl-type molecules exhibit superior detectability to X-rays, indicating the potential for significantly enhanced X-ray sensitivity through the development of modified molecules with enhanced electrical properties.

4. Experimental Section

A 1 mm thick glass substrate with a pre-deposited ITO layer (thickness of 100 nm with a sheet resistance of 25 Ω cm^{-2}, Merck KGaA) was employed to create molecular films on its surface, maintaining an equal surface area of 3.75 cm^2. A half surface of ITO was removed to prepare the bottom continuous electrode and an active molecular area was formed on top of it. The molecule material preparation and film production were done in a nitrogen chamber. A solution of the molecule powder in tetrahydrofuran (THF) was prepared at a concentration of 15 mg mL^{-1}. To achieve consistent film thickness, 300 µL of the prepared solutions were precisely drop-cast onto the entire area of each glass substrate using a micropipette. The substrates were then allowed to rest for 1 h, permitting the THF to fully evaporate. This resulted in a final layer with a thickness of ≈20 µm across all samples. Later the layers at the temperature of 70 °C (similar to the boiling point of THF) were left to dry out for 24 h to eliminate any trapped solvent. After the solvent elimination, the top aluminum electrode (40 nm thick) was vacuum evaporated by mask enclosure which formed the circle-shaped electrodes (⌀ 3 mm) on the active area with the path to form a reliable connection to the measurement scheme. Each substrate had dimensions of 15 mm × 25 mm, allowing for five electrodes with an area of 0.07 cm^2 to be placed on each substrate. Note that the vacuum-evaporated aluminum work function was 4.2 eV, while the bottom electrode's (ITO) was 4.7 eV. The wires were glued to the electrodes by silver-filled, electrically conductive adhesive and the samples were covered with a paraffin film (Parafilm "M"). The final samples were kept in a nitrogen atmosphere and in the dark to reduce oxidative effects.

The measurements of current–voltage (*I–V*) characteristics were performed by applying a voltage on the ITO electrode and measuring the induced current through the Al electrode using a transimpedance amplifier with a 1 GΩ feedback resistor (AMP in Figure 1). The X-ray photocurrent of a layer was obtained by irradiation using a molybdenum target X-ray tube under 35 kV (anode current 1 mA), which induced the 17.5 keV K_α characteristic irradiation in the middle of the continuous spectrum of bremsstrahlung radiation. The distance between the X-ray source and the sample was 10 cm for all measurements. In such conditions, the photon count (X-ray flux) at the surface of a layer was 6.5×10^9 cm^{-2} s^{-1}. The part of this flux caused by characteristic K_α and K_β radiation was equal to 2.7×10^9 cm^{-2} s^{-1}. The remaining part (3.8×10^9 cm^{-2} s^{-1}) was caused by bremsstrahlung.

A classical carbazolyl-containing oligoether poly[9-(2,3-epoxypropyl)-carbazole] (PEPK) was produced by the Latvian company "Biolar." The oligomer (M_w from 1000 to 1500) was prepared by the anionic oligomerization of the monomer. The glass transition temperature of the oligomer of such molecular weight was 65–75 °C.[73]

Well-defined branched carbazolyl-containing molecular glasses bis-{4,4'-[6-(carbazol-9-yl)-6-(carbazol-9-methyl)-2-hydroxy-4-oxahexylthia]-phenyl}sulfide (KOS), 1,3-bis[5-(3,6-dibromocarbazol-9-methyl)-6-(carbazol-9-yl)-2-hydroxy-4-oxahexyloxy]benzene (4Br-KOO), bis{4,4'-[6-(3,6-dibromocarbazol-9-yl)-5-(3,6-dibromocarbazol-9-methyl)-2-hydroxy-4-oxahexylthia]-phenyl}sulfide (8Br-KOS), and *N*,*N*-bis[6-(3,6-dibromocarbazol-9-yl)-5-(3,6-dibromocarbazol-9-methyl)-2-hydroxy-4-oxahexyl]-4-fluoroaniline (8Br-KONF) were prepared by the nucleophilic opening of the oxirane ring of glycidyl ethers of 1,3-di(carbazol-9-yl)-2-propanol, 1-(3,6-dibromocarbazol-9-yl)-3-(carbazol-9-yl)-2-propanol, and 1,3-di(3,6-dibromocarbazol-9-yl)-2-propanol with bis(4-mercaptophenyl)sulfide, 1,3-benzenediol, and 4-fluoroaniline. Synthesis and properties details are presented in refs. [52–54]. X-ray diffraction patterns of these compounds showed only broad halos which defined them as amorphous glasses. The glass transition temperatures (T_g) of the compounds KOS, 4Br-KOO, 8Br-KOS, and 8Br-KONF established by a differential scanning calorimetric method (DSC) were 90, 96, 115, and 118 °C, respectively.

Star-shaped charge-transporting materials tris[4-(2,2-diphenylethenyl)phenyl]amine (3TPA) and *N*, *N*-bis[4-(2,2-diphenylethenyl)-phenyl]-4-methylaniline (2TPA) containing a triphenylamine core and various phenylethenyl side arms were obtained in a one-step synthetic procedure by condensation of the appropriate triphenylamine derivatives with diphenylacetaldehyde in the presence of (±)-camphor-10-sulfonic acid. The glass transition temperatures (T_g) of the compounds 3TPA and 2TPA established by the DSC method were 98 and 73 °C, respectively. Synthesis and properties details are presented in refs. [74, 75].

For the synthesis of *N*,*N*-bis[6-(carbazol-9-yl)-5-(carbazol-9-methyl)-2-hydroxy-4-oxahexyl]-4-fluoroaniline (KONF), the mixture of glycidyl ethers of 1,3-di(carbazol-9-yl)-2-propanol (33.6 g, 0.075 mol), 4-fluoroaniline (3.3 g, 0.03 mol), and 5 mL of chlorobenzene was stirred at 140–145 °C. The temperature of the reaction mixture was increased to 165–170 °C when the 4-fluoroaniline disappeared. After termination of the reaction (20 h, TLC control), the product was purified by column chromatography with *n*-hexane/acetone (4:1, v/v) as the eluent and followed pouring of 20% solution in toluene into a tenfold excess of *n*-hexane. The precipitate was filtered off and washed with *n*-hexa-ne to afford KONF (25.0 g, 83%) as a white solid, $T_g = 95$ °C.

N,*N*-bis[6-(3,6-dibromocarbazol-9-yl)-5-(diphenylamino-*N*-methyl)-2-hydroxy-4-oxahexyl]aniline (4Br-KPON) were synthesized with the mixture of glycidyl ethers of 3-(3,6-dibromocarbazol-9-yl)-1-diphenylamino-2-propanol (15.2 g, 0.025 mol), aniline (0.9 g, 0.01 mol) and 3 mL of chlorobenzene was stirred at 175–180 °C. After termination of the reaction (45 h, TLC control), the product was purified by column chromatography with *n*-hexane/acetone (4:1, v/v) as the eluent and followed pouring of 20% solution in toluene into a tenfold excess of *n*-hexane. The precipitate was filtered off and washed with *n*-hexane to afford 4Br-KPON (9.8 g, 75.4%) as a white solid, $T_g = 92$ °C.

To measure the drift mobility of charge carriers in organic compounds, the xerographic time-of-flight (XTOF) technique was employed. Samples were fabricated by drop-casting onto aluminum-coated glass slides using THF as a solvent, with a thickness of 3–10 µm. An electric field was generated within the organic compound layer using corona charging. Charge carriers were introduced into the layer by illuminating it with nitrogen laser pulses (1 ns pulse duration, 337 nm wavelength). Small charge transients were measured using a wide-frequency band electrometer and oscilloscope. The transit time was extracted from the kink on the transient curve, either in linear or double logarithmic scale, depending on the charge

Table 2. Properties of the materials and films.

Material	2TPA	3TPA	KONF	KOS	4Br-KPON	4Br-KOO	8Br-KONF	8Br-KOS	PEPK
LUMO [eV]	−2.3	−2.3	−2.5	−2	−2.3	−2	−2.3	−2.4	−2.8
HOMO [eV]	−5.1	−5.1	−5.8	−5.8	−5.9	−5.7	−6	−6	−6
Eg [eV]	2.8	2.8	3.3	3.8	3.6	3.7	3.7	3.6	3.2
μ [cm^2 Vs^{-1}] (at 10^6 V cm^{-1})	2.4×10^{-2}	2.2×10^{-2}	5×10^{-5}	6×10^{-5}	10^{-6}	9×10^{-5}	$<10^{-6}$	5×10^{-6}	4×10^{-5}
Film thickness [µm]	25.8	25.4	23.3	21.8	19.3	24.4	19.9	20.2	25
A [GeV s^{-1}]	6.91	6.79	7.38	19.6	211	266	385	373	7.50
Absorbed dose rate [mGy s^{-1}]	5.06	5.05	6.03	17.1	181	181	285	272	5.78

transport mechanism (Gaussian or dispersive). Drift mobility was calculated using the formula

$$\mu = d^2/U_0 t_t \tag{3}$$

where d is the layer thickness, U_0 is the surface potential, and t_t is transit time.

A combination of electron photoemission spectroscopy (PES) and optical absorption spectroscopy was employed to determine the ionization potential (I_p), HOMO, LUMO, and band gap energies of organic compounds. PES involved irradiating a sample with UV light from a He discharge lamp, causing the emission of photoelectrons with kinetic energies proportional to the incident radiation.[52,76] The I_p was identified as the threshold energy at which photoelectron emission occurred. The HOMO level was equated to the I_p, while the LUMO energy was calculated by adding the I_p to the optical energy gap (E_{opt}). To ensure accurate I_p measurements, an air chamber was employed, mimicking a Geiger–Muller counter[77] to register every emitted photoelectron. This approach eliminated the need for corrections due to secondary electron emission, enhancing the accuracy of I_p values compared to vacuum-based PES systems. Optical absorption spectra were measured using a spectrophotometer Perkin Elmer Lambda 850. The band gap energy, which represented the energy required to promote an electron from the HOMO to the LUMO, was determined from the onset of absorption in the optical spectrum. These parameters, along with the ionization potential and HOMO-LUMO energies, provided valuable insights into the material's electronic properties for electronics applications (**Table 2**).

X-ray sensitivity was determined by dividing the experimental photocurrent density (measured at 300 V) by the calculated absorbed dose rate in air, which was equal to 13.3 mGy s^{-1}. This dose rate was calculated using the known spectrum and intensity of incident radiation and the elemental composition of dry air (taken from the "Earth Fact Sheet" by NASA, https://nssdc.gsfc.nasa.gov/planetary/factsheet/earthfact.html).

The detection limit of a device is defined as the ratio of the minimum detectable photocurrent density to the X-ray sensitivity defined above. That is to say, it is the smallest detectable dose rate in air. The minimum detectable photocurrent density is the ratio of the minimum detectable photocurrent (I_d) to the device area that is exposed to incident radiation. I_d depends both on statistics of charge carrier generation in the material and on the sensitivity of the device used to measure the current. In the present work, the latter factor was the limiting one.

The smallest detectable difference between photocurrent and dark current can be determined by the noise of the measured current. The current noise in the measurement time range of 0.5 to 40 s varied between samples. Its value fell within the range of 0.25 to 1 pA.

In order to calculate the theoretical saturation value of the photocurrent ($I_{ph.th}$), the photogeneration rate Φ was calculated, which is by definition equal to

$$\Phi = \frac{A}{W} \tag{4}$$

where A is the energy absorption rate (i.e., the energy absorbed in the sample per unit time), and W is the "W value" of the material (i.e., the average energy of incident X-ray radiation absorbed in the sample per one created electron–hole pair). The value of A can be easily calculated by applying two assumptions: a) photoelectric absorption is the only type of interaction between the incident X-ray radiation and the target material, and b) there is no secondary radiation escaping the sample after a photoelectric absorption event (i.e., any secondary radiation is completely absorbed in the sample material). In such a case, the only parameters needed for calculation of A are the spectrum and intensity of the incident radiation, the set of tabulated values of photoelectric absorption cross sections for all chemical elements composing the sample on a sufficiently dense energy grid spanning the entire range of X-ray photon energies (in the case discussed—from ≈5 to 35 keV), and the total number of atoms of each chemical element in the active area of the sample (keeping in mind that X-ray radiation is incident normally, and X-ray flux is uniform over the entire surface of the sample). All those parameters are known. Then, if absorption is sufficiently weak (so that photogeneration is practically uniform over the entire sample), the value of A can be calculated as follows

$$A = \sum_Z N_Z \int_0^\infty \sigma(Z, E)\, P(E)\, E dE \tag{5}$$

where N_Z is the total number of atoms of chemical element with atomic number Z in the active area of the sample, E is the photon energy, $\sigma(Z, E)$ is the photoelectric absorption cross section at photon energy E for chemical element No. Z, and $P(E)$ is the spectral photon flux density (i.e., number of photons with energy E per unit area per unit energy per unit time). It is important to note that these calculations do not require any information about chemical bonds between atoms: only the total quantities of each element are needed. This is because photoelectric absorption occurs due to the interaction of the incident X-ray photon with an inner-shell electron, which is ejected (usually from the innermost K shell of the atom), and the inner shells are practically undisturbed by the formation of chemical bonds between atoms. Hence, the material can be treated as a collection of non-interacting neutral atoms.

In many cases, the above expression of A is accurate to a few percent. However, if elements with sufficiently large values of Z are present in the sample in sufficient quantities, this value of A may be overestimated by more than 30%. This error is mainly caused by the inaccuracy of the second-mentioned assumption (about complete absorption of secondary radiation). The main type of secondary radiation after a photoelectric absorption event is the emission of a characteristic X-ray photon due to the filling of the vacancy created in the K shell of the atom (this X-ray radiation is called "X-ray fluorescence"). Since the photon energy of this secondary radiation increases with increasing Z, and since the values of $\sigma(Z, E)$ decrease rapidly with increasing E (i.e., $\sigma \sim E^{-3}$), the fraction of X-ray fluorescence photons escaping the sample increases rapidly with Z. It should be noted that the mentioned fast increase of the photoelectric absorption

cross section with increasing Z (i.e., $\sigma \sim Z^5$) makes it possible that even a small quantity of a high-Z element present in the material has a predominant role in the photoelectric absorption process, leading to disproportionally large energy losses due to X-ray fluorescence. For example, in the four mentioned materials that include Br, practically all photoelectric absorption occurs in Br atoms, and more than 30% of absorbed incident radiation is re-emitted from the sample in the form of X-ray fluorescence (photon energies of K_α and K_β spectral lines of characteristic X-ray radiation of Br atoms are equal to 11.9 and 13.29 keV, respectively). In order to take into account this effect, the value of A was calculated in the present work by Monte Carlo simulation. In comparison with the previously described method of calculating A, the Monte Carlo estimate is more accurate, because it takes into account various additional effects. Accordingly, the method of Monte Carlo simulation requires more detailed cross-section data: not only photoelectric cross-sections, but also cross-sections of other types of photon interactions (coherent scattering and Compton scattering), cross-sections of electron interactions (elastic scattering, impact ionization, and bremsstrahlung), angular distributions of secondary particles produced in each type of interaction (because all secondary photons and electrons are tracked until their absorption or escape from the sample, and all possible their interactions with atoms are simulated), and probabilities of transitions between different electronic sub-shells of an atom (after the mentioned vacancy is created in an inner shell of an atom). However, the mentioned approximation of non-interacting neutral atoms is acceptable for a Monte Carlo simulation, too, because the main contribution to the value of A comes from relatively high-energy photons and electrons (with energy of the order of a few keV or greater), and in this energy range the role of valence electrons (and of the chemical bonds between atoms) is not important. Low-energy electrons and photons are practically completely absorbed inside the sample so that inaccuracies of their cross sections (caused by the mentioned neglect of interactions between atoms) have no effect. Those inaccuracies affect only the detailed sequence of collisions experienced by each low-energy electron, but not the total energy deposited by it in the sample (this energy is simply the initial energy of the electron, because it was completely stopped inside the sample). In contrast, high-energy photons and electrons have a much higher probability to escape the sample, hence their interactions must be simulated accurately, in order to make the estimate of the energy loss caused by their escape as accurate as possible. The cross sections of atomic interactions of electrons and photons, which were used for the Monte Carlo simulations in the present work, were taken from Evaluated Electron Data Library (EEDL)[78] and the evaluated photo data library (EPDL),[79] respectively, and the atomic relaxation data were taken from Evaluated Atomic Data Library (EADL),[80] The values of A calculated by Monte Carlo simulation are given in Table 2.

Another quantity, which is needed to calculate the photogeneration rate Φ, is the W value of the material. It was determined empirically that the W value of a semiconductor is approximately proportional to its bandgap E_g

$$W = f E_g \tag{6}$$

where the factor f is approximately equal to 2.8 for crystalline Si and Ge,[81] and approximately equal to 2.2 for amorphous Se.[82] Although this proportionality relation between W and E_g was obtained for inorganic semiconductors, it is likely that a similar relation holds for organic semiconductors (such as those discussed in the present work), too. However, the proportionality factor f may be different from the mentioned values. Since the minimum possible value of this factor is equal to 1, and since its maximum value for inorganic semiconductors is approximately equal to 3, it seems that an estimate of the photogeneration rate with a relative uncertainty of ±50% can be obtained by assuming that $f \approx 2$, that is, $W \approx 2E_g$. In such a case, the photogeneration rate is equal to

$$\Phi = \frac{A}{2E_g} \tag{7}$$

The values of E_g and A are given in Table 2. The values of $I_{ph.th}$ calculated using the above expression of Φ are given in Table 1.

Statistical analysis of all Monte Carlo simulations was performed using 6.5×10^6 incident photons. This number is sufficiently large to ensure a relative error of less than 5×10^{-4} (i.e., three-digit precision) in Monte Carlo estimates of absorbed dose and maximum photocurrent.

Acknowledgements

This research was carried out in the framework of the "Universities' Excellence Initiative" program by the Ministry of Education, Science, and Sports of the Republic of Lithuania under the agreement with the Research Council of Lithuania (project No. S-A-UEI-23-6) and was funded by the Research Council of Lithuania grant No. S-MIP-22-8.

Conflict of Interest

The authors declare no conflict of interest.

Data Availability Statement

The data that support the findings of this study are available from the corresponding author upon reasonable request.

Keywords

direct X-ray sensors, triphenylamine-carbazolyl-containing molecules

Received: February 3, 2024
Revised: March 17, 2024
Published online: May 6, 2024

[1] M. Cordella, F. Alfieri, J. Sanfelix, *J. Ind. Ecol.* **2021**, *25*, 448.
[2] M. Sloma, in Electron Technology Conf. 2013 (Eds: P. Szczepanski, R. Kisiel, R. S. Romaniuk), SPIE, Bellingham, WA **2013**, pp. 541–548.
[3] L. Cabernard, S. Pfister, C. Oberschelp, S. Hellweg, *Nat. Sustainability* **2022**, *5*, 139.
[4] É. Bozó, H. Ervasti, N. Halonen, S. H. H. Shokouh, J. Tolvanen, O. Pitkänen, T. Järvinen, P. S. Pálvölgyi, Á. Szamosvölgyi, A. Sápi, Z. Konya, M. Zaccone, L. Montalbano, L. De Brauwer, R. Nair, V. Martínez-Nogués, L. San Vicente Laurent, T. Dietrich, L. Fernández de Castro, K. Kordas, *ACS Appl. Mater. Interfaces* **2021**, *13*, 49301.
[5] I. McCulloch, M. Chabinyc, C. Brabec, C. B. Nielsen, S. E. Watkins, *Nat. Mater.* **2023**, *22*, 1304.
[6] I. Saikia, A. J. Borah, P. Phukan, *Chem. Rev.* **2016**, *116*, 6837.
[7] R. Rybakiewicz, M. Zagorska, A. Pron, *Chem. Pap.* **2017**, *71*, 243.
[8] A. Operamolla, A. Punzi, G. M. Farinola, *Asian J. Org. Chem.* **2017**, *6*, 120.
[9] Y. S. Kurniawan, K. T. A. Priyangga, P. A. Krisbiantoro, A. C. Imawan, *J. Multidiscip. Appl. Nat. Sci.* **2021**, *1*, 1.
[10] F. Catania, H. de S. Oliveira, P. Lugoda, G. Cantarella, N. Münzenrieder, *J. Phys. D: Appl. Phys.* **2022**, *55*, 323002.
[11] Z. Lin, Y. Huang, X. Duan, *Nat. Electron.* **2019**, *2*, 378.
[12] R. R. Søndergaard, M. Hösel, F. C. Krebs, *J. Polym. Sci., Part B: Polym. Phys.* **2013**, *51*, 16.
[13] R. Abbel, Y. Galagan, P. Groen, *Adv. Eng. Mater.* **2018**, *20*, 1701190.
[14] G. Liu, Z. Lv, S. Batool, M.-Z. Li, P. Zhao, L. Guo, Y. Wang, Y. Zhou, S.-T. Han, *Small* **2023**, *19*, 2207879.
[15] M. Qiu, A. Singh, D. Wang, J. Qu, M. Swihart, H. Zhang, P. N. Prasad, *Nano Today* **2019**, *25*, 135.

[16] T. Stockinger, B. Liedl, M. Steiner, R. Schwödiauer, F. Padinger, S. Bauer, M. Kaltenbrunner, U. Müller, *Sens. Actuators, B* **2020**, *324*, 128750.
[17] P. J. Statham, *J. Microsc.* **1981**, *123*, 1.
[18] T. Khalil, F. Monteiro, A. Dandache, C. Salame, *AIP Conf. Proc.* **2020**, *2307*, 020049.
[19] J. M. Jaklevic, F. S. Goulding, *IEEE Trans. Nucl. Sci.* **1971**, *18*, 187.
[20] S. O. Kasap, J. A. Rowlands, *J. Mater. Sci.: Mater. Electron.* **2000**, *11*, 179.
[21] F. Akbari, E. I. Parsai, D. Shvydka, in *High-Z Materials for X-ray Detection: Material Properties and Characterization Techniques*, (Eds: L. Abbene, K. (Kris) Iniewski), Springer International Publishing, Springer, New York **2023**, pp. 23–41.
[22] P. Lecoq, *Nucl. Instrum. Methods Phys. Res., Sect. A* **2016**, *809*, 130.
[23] H. O. Anger, *Rev. Sci. Instrum.* **1958**, *29*, 27.
[24] B. K. Cha, S. Jeon, C.-W. Seo, *Nucl. Instrum. Methods Phys. Res., Sect. A* **2016**, *831*, 404.
[25] X. Wang, H. Shi, H. Ma, W. Ye, L. Song, J. Zan, X. Yao, X. Ou, G. Yang, Z. Zhao, M. Singh, C. Lin, H. Wang, W. Jia, Q. Wang, J. Zhi, C. Dong, X. Jiang, Y. Tang, X. Xie, Y. (Michael) Yang, J. Wang, Q. Chen, Y. Wang, H. Yang, G. Zhang, Z. An, X. Liu, W. Huang, *Nat. Photonics* **2021**, *15*, 187.
[26] Y. Wu, J. Feng, Z. Yang, Y. Liu, S. (Frank) Liu, *Adv. Sci.* **2023**, *10*, 2205536.
[27] M. Chen, C. Wang, W. Hu, *J. Mater. Chem. C* **2021**, *9*, 4709.
[28] J.-K. Chen, N. Shirahata, H.-T. Sun, *Nat. Photonics* **2021**, *15*, 171.
[29] X. Yu, J. Mi, Y. Han, C. Sun, M. Wang, G. Guo, *Chin. Chem. Lett.* **2023**, 109233.
[30] H. Li, Y. Lei, G. Peng, Q. Wang, Z. Li, H. Wang, G. Wang, Z. Jin, *Adv. Funct. Mater.* **2022**, *32*, 2208199.
[31] I. Temiño, L. Basiricò, I. Fratelli, A. Tamayo, A. Ciavatti, M. Mas-Torrent, B. Fraboni, *Nat. Commun.* **2020**, *11*, 2136.
[32] W.-F. Wang, J. Lu, X.-M. Xu, B.-Y. Li, J. Gao, M.-J. Xie, S.-H. Wang, F.-K. Zheng, G.-C. Guo, *Chem. Eng. J.* **2022**, *430*, 133010.
[33] M. Chen, L. Sun, X. Ou, H. Yang, X. Liu, H. Dong, W. Hu, X. Duan, *Adv. Mater.* **2021**, *33*, 2104749.
[34] J. W. Kingsley, S. J. Weston, D. G. Lidzey, *IEEE J. Sel. Top. Quantum Electron.* **2010**, *16*, 1770.
[35] L. Basiricò, A. Ciavatti, I. Fratelli, D. Dreossi, G. Tromba, S. Lai, P. Cosseddu, A. Bonfiglio, F. Mariotti, C. Dalla Val, V. Bellucci, J. E. Anthony, B. Fraboni, *Front. Phys.* **2020**, *8*, 13.
[36] D. Vikraman, H. Liu, S. Hussain, K. Karuppasamy, H.-K. Youi, J. Jung, J. Kang, H.-S. Kim, *Appl. Surf. Sci.* **2021**, *543*, 148863.
[37] Z. Li, S. Chang, H. Zhang, Y. Hu, Y. Huang, L. Au, S. Ren, *Nano Lett.* **2021**, *21*, 6983.
[38] A. J. J. M. van Breemen, M. Simon, O. Tousignant, S. Shanmugam, J.-L. van der Steen, H. B. Akkerman, A. Kronemeijer, W. Ruetten, R. Raaijmakers, L. Alving, J. Jacobs, P. E. Malinowski, F. De Roose, G. H. Gelinck, *npj Flexible Electron.* **2020**, *4*, 22.
[39] L. Basiricò, A. Ciavatti, B. Fraboni, *Adv. Mater. Technol.* **2021**, *6*, 2000475.
[40] M. P. A. Nanayakkara, L. Matjačić, S. Wood, F. Richheimer, F. A. Castro, S. Jenatsch, S. Züfle, R. Kilbride, A. J. Parnell, M. G. Masteghin, H. M. Thirimanne, A. Nisbet, K. D. G. I. Jayawardena, S. R. P. Silva, *Adv. Funct. Mater.* **2021**, *31*, 2008482.
[41] S. Lai, P. Cosseddu, L. Basiricò, A. Ciavatti, B. Fraboni, A. Bonfiglio, *Adv. Electron. Mater.* **2017**, *3*, 1600409.
[42] D. Adliene, B. G. Urbonavicius, J. Laurikaitiene, J. Puiso, *Radiat. Phys. Chem.* **2020**, *168*, 108609.
[43] A. U. Alam, Y. Qin, S. Nambiar, J. T. W. Yeow, M. M. R. Howlader, N.-X. Hu, M. J. Deen, *Prog. Mater. Sci.* **2018**, *96*, 174.
[44] A. M. Zeidell, T. Ren, D. S. Filston, H. F. Iqbal, E. Holland, J. D. Bourland, J. E. Anthony, O. D. Jurchescu, *Adv. Sci.* **2020**, *7*, 2001522.
[45] I.-A. Ratiu, V. Bocos-Bintintan, F. Monedeiro, M. Milanowski, T. Ligor, B. Buszewski, *Crit. Rev. Anal. Chem.* **2020**, *50*, 501.
[46] M. Y. Lee, H. R. Lee, C. H. Park, S. G. Han, J. H. Oh, *Acc. Chem. Res.* **2018**, *51*, 2829.
[47] X. Fang, B. Zong, S. Mao, *Nano-Micro Lett.* **2018**, *10*, 64.
[48] J. Heller, D. Lyman, W. Hewett, *Makromol. Chem.* **1963**, *73*, 48.
[49] P. Strohriegl, J. V. Grazulevicius, in *Handbook of Organic Conductive Molecules and Polymers: Charge-Transfer Salts, Fullerenes, and Photoconductors*, 1st ed., Vol. *1* (Ed: H. S. Nalwa), Wiley, New York **1997**, p. 553.
[50] J. V. Grazulevicius, P. Strohriegl, J. Pielichowski, K. Pielichowski, *Prog. Polym. Sci.* **2003**, *28*, 1297.
[51] V. Gaidelis, V. Kriščiūnas, E. Montrimas, *Thin Solid Films* **1976**, *38*, 9.
[52] M. Daskeviciene, V. Getautis, J. V. Grazulevicius, A. Stanisauskaite, J. Antulis, V. Gaidelis, V. Jankauskas, J. Sidaravicius, *J. Imaging Sci. Technol.* **2002**, *46*, 467.
[53] S. Kutkevicius, A. Stanisauskaite, V. Getautis, A. Railaite, S. Uss, *J. Prakt. Chem.* **1995**, *337*, 315.
[54] D. Tomkute-Luksiene, T. Malinauskas, M. Daskeviciene, V. Gaidelis, R. Maldzius, J. Sidaravicius, V. Getautis, *Synth. Met.* **2011**, *161*, 1177.
[55] P. Russo, *Handbook of X-ray Imaging: Physics and Technology*, CRC Press, Boca Raton, FL **2017**.
[56] S. Kasap, J. B. Frey, G. Belev, O. Tousignant, H. Mani, J. Greenspan, L. Laperriere, O. Bubon, A. Reznik, G. DeCrescenzo, K. S. Karim, J. A. Rowlands, *Sensors* **2011**, *11*, 5112.
[57] S. Svanström, A. G. Fernández, T. Sloboda, T. Jesper Jacobsson, H. Rensmo, U. B. Cappel, *Phys. Chem. Chem. Phys.* **2021**, *23*, 12479.
[58] S. Akhter, K. Allan, D. Buchanan, J. A. Cook, A. Campion, J. M. White, *Appl. Surf. Sci.* **1988**, *35*, 241.
[59] F. Maye, A. Turak, *Radiation* **2021**, *1*, 131.
[60] H.-C. Hu, H.-S. Hu, B. Zhao, P. Cui, P. Cheng, J. Li, *Angew. Chem., Int. Ed.* **2015**, *54*, 11681.
[61] D. Cantillo, C. O. Kappe, *React. Chem. Eng.* **2017**, *2*, 7.
[62] A. Hassan, N. Das, *ACS Appl. Polym. Mater.* **2023**, *5*, 5349.
[63] F. Dumur, L. Beouch, S. Peralta, G. Wantz, F. Goubard, D. Gigmes, *Org. Electron.* **2015**, *25*, 21.
[64] C. Garcias-Morales, D. Romero-Borja, J.-L. Maldonado, A. Roa, M. Rodríguez, J. García-Merinos, A. Ariza-Castolo, *Molecules* **2017**, *22*, 1607.
[65] K. A. Khalaph, Z. J. Shanan, A. M. Jafar, F. M. Al-Attar, *DDF* **2020**, *398*, 140.
[66] C. W. Han, Y. H. Tak, in *Flat Panel Display Manufacturing*, John Wiley & Sons, Ltd, Hoboken, NJ **2018**, pp. 143–158.
[67] G. Zhang, S. A. Hawks, C. Ngo, L. T. Schelhas, D. T. Scholes, H. Kang, J. C. Aguirre, S. H. Tolbert, B. J. Schwartz, *ACS Appl. Mater. Interfaces* **2015**, *7*, 25247.
[68] R. Dobužinskas, A. Poškus, M. Viliūnas, V. Jankauskas, M. Daškevičienė, V. Getautis, K. Arlauskas, *Phys. Status Solidi A* **2019**, *216*, 1900635.
[69] M. Bagatin, S. Gerardin, *Ionizing Radiation Effects in Electronics: From Memories to Imagers*, Taylor & Francis, London **2015**.
[70] M. J. Berger, J. H. Hubbell, S. M. Seltzer, J. Chang, J. S. Coursey, R. Sukumar, D. S. Zucker, K. Olsen, XCOM: Photon Cross Section Database (version 1.5), National Institute of Standards and Technology, Gaithersburg, MD **2010**, [Online] Available: https://physics.nist.gov/xcom.
[71] H. M. Thirimanne, K. D. G. I. Jayawardena, A. J. Parnell, R. M. I. Bandara, A. Karalasingam, S. Pani, J. E. Huerdler, D. G. Lidzey, S. F. Tedde, A. Nisbet, C. A. Mills, S. R. P. Silva, *Nat. Commun.* **2018**, *9*, 2926.
[72] C. Ji, S. Wang, Y. Wang, H. Chen, L. Li, Z. Sun, Y. Sui, S. Wang, J. Luo, *Adv. Funct. Mater.* **2020**, *30*, 1905529.

[73] A. Undzėnas, V. Gaidelis, J. Sidaravičius, R. Kavoliūnas, J. Zdanavicius, *Electrophotographic material poly[9-(2,3-epoxypropyl)carbazole] (PEPK)*, **1976** Chem. Commun.
[74] T. Malinauskas, D. Tomkute-Luksiene, M. Daskeviciene, V. Jankauskas, G. Juska, V. Gaidelis, K. Arlauskas, V. Getautis, *Chem. Commun.* **2011**, *47*, 7770.
[75] T. Malinauskas, M. Daskeviciene, G. Bubniene, I. Petrikyte, S. Raisys, K. Kazlauskas, V. Gaidelis, V. Jankauskas, R. Maldzius, S. Jursenas, V. Getautis, *Chemistry* **2013**, *19*, 15044.
[76] E. Miyamoto, Y. Yamaguchi, M. Yokoyama, *Electrophotography* **1989**, *28*, 364.
[77] H. Geiger, W. Müller, *Naturwissenschaften* **1928**, *16*, 617.
[78] S. T. Perkins, D. E. Cullen, M. H. Chen, J. Rathkopf, J. Scofield, J. H. Hubbell, Tables and graphs of atomic subshell and relaxation data derived from the LLNL Evaluated Atomic Data Library (EADL), Z = 1–100 **1991**, Office of Scientific and Technical Information (OSTI), https://doi.org/10.2172/10121422.
[79] D. E. Cullen, J. H. Hubbell, L. Kissel, EPDL97: the evaluated photo data library '97 version. **1997**, Office of Scientific and Technical Information (OSTI). https://doi.org/10.2172/295438.
[80] S. T. Perkins, D. E. Cullen, M. H. Chen, J. Rathkopf, J. Scofield, J. H. Hubbell, *Lawrence Livermore Lab., [Rep.] UCRL* **1991**, *30*, 1991.
[81] C. A. Klein, *J. Appl. Phys.* **2003**, *39*, 2029.
[82] W. Que, J. A. Rowlands, *Phys. Rev. B* **1995**, *51*, 10500.